

# THE CONNECTION BETWEEN THERMAL AND NON-THERMAL EMISSION IN GAMMA-RAY BURSTS: GENERAL CONSIDERATIONS AND GRB090902B AS A CASE STUDY

ASAF PE'ER<sup>1,2</sup>, BIN-BIN ZHANG<sup>3</sup>, FELIX RYDE<sup>4</sup>, SINÉAD MCGLYNN<sup>4</sup>, BING ZHANG<sup>3</sup>, ROBERT D. PREECE<sup>5</sup>, CHRYSIA KOUVELIOTOU<sup>6</sup>

*Draft version April 28, 2022*

## ABSTRACT

Photospheric (thermal) emission is inherent to the gamma-ray burst (GRB) “fireball” model. We show here, that inclusion of this component in the analysis of the GRB prompt emission phase naturally explains some of the prompt GRB spectra seen by the *Fermi* satellite over its entire energy band. The sub-MeV peak is explained as multi-color black body emission, and the high energy tail, extending up to the GeV band, results from roughly similar contributions of synchrotron emission, synchrotron self Compton (SSC) and Comptonization of the thermal photons by energetic electrons originating after dissipation of the kinetic energy above the photosphere. We show how this analysis method results in a complete, self consistent picture of the physical conditions at both emission sites of the thermal and non-thermal radiation. We study the connection between the thermal and non-thermal parts of the spectrum, and show how the values of the free model parameters are deduced from the data. We demonstrate our analysis method on GRB090902B: We deduce a Lorentz factor in the range  $780 \leq \eta \leq 1000$ , photospheric radius  $r_{ph} \simeq 6.1 - 7.8 \times 10^{11}$  cm and dissipation radius  $r_\gamma \geq 3.8 - 5.0 \times 10^{15}$  cm. By comparison to afterglow data, we deduce that a large fraction,  $\epsilon_d \approx 85\% - 95\%$  of the kinetic energy is dissipated, and that large fraction,  $\sim$  equipartition of this energy is carried by the electrons and the magnetic field. This high value of  $\epsilon_d$  questions the “internal shock” scenario as the main energy dissipation mechanism for this GRB.

*Subject headings:* gamma rays:bursts—gamma rays:theory—plasmas—radiation mechanisms:thermal—radiative transfer—scattering

## 1. INTRODUCTION

Although extensively studied for nearly two decades, the origin of the prompt emission of gamma-ray bursts (GRBs) is still puzzling. Up until these days, GRB prompt emission spectra are often modelled as a smoothly broken power-law, which is referred to as the “Band” function (Band *et al.* 1993; Preece *et al.* 1998a, 2000; Kaneko *et al.* 2006, 2008; Abdo *et al.* 2009b). While the “Band” function often provides very good fits to the observed spectra over a limited energy range, it suffers two crucial drawbacks. In several bursts seen by the *Fermi* satellite, a high energy tail extending up to tens of GeV was seen (e.g., GRB090510, Ackerman *et al.* (2010); or GRB090902B, Abdo *et al.* (2009a)). The first drawback is that this tail requires more than the “Band” function on its own to have an acceptable fit. However, the most severe drawback is that the “Band” function, being empirical in nature, does not provide any information about the emission mechanism that produces the prompt radiation.

A common interpretation of the observed GRB spectrum is that it results from synchrotron emission, ac-

companied perhaps by synchrotron-self Compton (SSC) emission at high energies (Rees & Mészáros 1994; Sari & Piran 1997; Pilla & Loeb 1998; Guetta & Granot 2003a; Pe'er & Waxman 2004). The emission follows the dissipation of a kinetic energy. The two prevalent dissipation models involve either internal shocks (Rees & Mészáros 1994; Sari & Piran 1997b), or magnetic energy dissipation in Poynting dominated outflows (Thompson 1994; Spruit *et al.* 2001; Giannios & Spruit 2005; Zhang & Yan 2010). These models have two main advantages. First, they can explain the complex lightcurves often seen (albeit with very little predictive power). Second, they naturally account for the non-thermal spectrum.

In spite of these advantages, in recent years evidence is accumulating for serious difficulties in these models. A well known deficiency of the internal shock scenario is the low efficiency of energy conversion (Mochkovich *et al.* 1995; Kobayashi *et al.* 1997; Lazzati *et al.* 1999; Guetta *et al.* 2001), resulting from the fact that only the energy associated with the differential motion between the expanding ejecta shells after the GRB explosion can be dissipated, and that this energy is much lower than the energy associated with the bulk motion. This is in contrast to the observations which show high efficiency in  $\gamma$ -ray emission, of the order of tens of percent (Zhang *et al.* 2007; Nysewander *et al.* 2009). A second drawback is that optically thin synchrotron and SSC emission cannot account for the steepness of the low energy spectral slopes (Crider *et al.* 1997; Preece *et al.* 1998b, 2002; Ghirlanda *et al.* 2003) (although part of the observed steepening may be accounted for when SSC in the Klein Nishina limit is considered; see Daigne *et al.* 2009).

<sup>1</sup> Space Telescope Science Institute, 3700 San Martin Dr., Baltimore, Md, 21218; apeer@stsci.edu

<sup>2</sup> Giacconi Fellow

<sup>3</sup> Department of Physics and Astronomy, University of Nevada, Las Vegas, NV 89154

<sup>4</sup> Department of Physics, Royal Institute of Technology, AlbaNova, SE-106 91 Stockholm, Sweden

<sup>5</sup> Center for Space Plasma and Aeronomic Research (CSPAR), University of Alabama in Huntsville, Huntsville, AL 35899, USA

<sup>6</sup> Space Science Office, VP62, NASA/Marshall Space Flight Center, Huntsville, AL 35812, USA

Third, the high energy spectral slope varies significantly from burst to burst (Preece *et al.* 1998a; Kaneko *et al.* 2006), with some bursts showing very steep high energy spectral slopes. This is in contradiction to the expected spectral slope of synchrotron emission from a power law distribution of electrons, which is expected to produce a fairly constant spectrum,  $\nu F_\nu \propto \nu^0$ . Finally, the fitting is often made to the *time integrated* spectrum. Analysis of *time resolved* spectra done by Crider *et al.* (1998) and Ghirlanda *et al.* (2003), has shown that neither the synchrotron nor the SSC models can explain the time resolved low energy spectral slopes.

These well known difficulties of the synchrotron emission model have motivated the study of alternative scenarios. These include, among others, quasi-thermal Comptonization (Ghisellini & Celotti 1999), Compton drag (Zdziarski *et al.* 1991; Shemi 1994; Lazzati *et al.* 2000), jitter radiation (Medvedev 2000), Compton scattering of synchrotron self absorbed photons (Panaitescu & Mészáros 2000; Stern & Poutanen 2004) and synchrotron emission from a decaying magnetic field (Pe'er & Zhang 2006).

An alternative model, which is arguably the most natural one, is a radiative contribution from the photosphere (Eichler & Levinson 2000; Mészáros & Rees 2000; Mészáros *et al.* 2002; Daigne & Mochkovitch 2002; Rees & Mészáros 2005). Indeed, a photospheric emission is a natural outcome of the “fireball” model. At small radii, close to the inner engine, the optical depth is huge,  $\tau \sim 10^{15}$  (see, e.g., Piran 2005, for a review). As a result, photons cannot escape, but are advected with the flow until they decouple at the photosphere. The huge value of the optical depth implies that regardless of the initial emitted spectrum, if photons are emitted deep enough in the flow, the spectrum emerging at the photosphere is black-body (a Wien spectrum may be obtained if the number of photons is conserved). In fact, in the classical “fireball” model, photons serve as mediators for energy conversion (the explosion energy is converted into kinetic energy of the relativistically expanding plasma jet by scattering between photons and leptons, which in turn convert the energy to the baryons via Coulomb collisions). Therefore, the appearance of thermal photons as part of the observed spectrum is not only expected, but is in fact *required*.

Apart from being an inherent part of the “fireball” model, one of the key advantages of the idea that at least part of the observed spectrum originates from the photosphere is that it provides a relief for the efficiency problem of the internal shock model (Pe'er *et al.* 2005; Ryde & Pe'er 2009; Lazzati *et al.* 2009). This is because only the non-thermal part of the spectrum is required to originate from energy dissipation above the photosphere. A second great advantage of this idea is that the Rayleigh-Jeans part of the thermal spectrum (or modification of it) can naturally account for low energy spectral slopes much steeper than those allowed by the synchrotron theory, and are hence consistent with observations.

The observed GRB spectra are therefore expected to be hybrid, i.e., containing both thermal and non-thermal parts. These two parts are connected in a non-trivial way. As the non-thermal part originates from energy dissipation (one or more) occurring above the photosphere, it is naturally delayed with respect to the thermal pho-

tons. A complete decomposition of the thermal and non-thermal parts of the spectrum is in fact nearly impossible. Thermal photons serve as seed photons to Compton scattering by the energetic electrons, thereby affecting the non-thermal part as well. Even if the dissipation occurs high above the photosphere, thermal photons significantly contribute to the cooling of the electrons (Pe'er *et al.* 2005), therefore affecting the spectrum emitted by these electrons. As was shown by Pe'er *et al.* (2006), under these conditions a flat energy spectrum ( $\nu F_\nu \propto \nu^0$ ), resulting from multiple Compton scattering of the thermal photons, is naturally obtained for a large range of parameters. A similar conclusion was drawn in the case of a magnetized outflow (Giannios 2006). These predictions were shown to be in qualitatively very good agreement with *Fermi* results (Toma *et al.* 2010).

The non-trivial connection between the thermal and non-thermal components, combined with the fact that both components vary in time, make it difficult to identify the thermal component. A breakthrough in identifying this component was made by Ryde (2004, 2005), who looked at *time resolved* spectra, thereby allowing an identification of the temporal evolution of the temperature. Repeating a similar analysis on a fairly large sample of bursts, it was shown by Ryde & Pe'er (2009) that the thermal component not only could be identified, but that both the temperature and flux of this component show repetitive, well defined temporal behaviour at late times:  $F_{BB}^{ob} \propto t^{-2}$ , and  $T^{ob} \propto t^{-2/3}$ . This behaviour was found to be in very good agreement with the theoretical predictions (Pe'er 2008), thereby providing an independent indication for the correct identification of the thermal emission component. It should be pointed out here, that the thermal emission is expected to appear as gray-body emission, composed of multi-color black body spectra. This results from the fact that at a given time interval, an observer sees photons emitted from different radii and different angles, hence undergoing different Doppler shifts. A full analysis shows that the resulting low energy spectrum (below the observed spectral peak, typically seen at sub MeV) is a power law [Pe'er & Ryde, in prep.].

Once the thermal component is identified, it is relatively easy to use its properties to deduce the dynamics of the outflow. As opposed to the non-thermal part, whose emission radius is uncertain (there may be multiple emission radii), the emission radius of the thermal photons is defined to be at the photosphere. Thus, by studying the properties (thermal flux and temperature) of the thermal component, under the assumption of constant outflow velocity, it is possible to deduce the photospheric radius and the Lorentz factor of the flow (Pe'er *et al.* 2007). We note that this method is independent, and is complementary to the opacity argument method commonly used to constrain the Lorentz factor of the flow at the emission radius of the high-energy photons (Svensson 1987; Krolik & Pier 1991; Woods & Loeb 1995; Lithwick & Sari 2001). It has two main advantages to the opacity argument method. First, it provides a direct measurement of the Lorentz factor, rather than a lower limit. Second, it is independent of measurements of the variability time, which is highly uncertain.

While in the past a clear identification of a ther-

mal component was difficult, the situation dramatically changed with the broad band spectral coverage enabled with the launch of *Fermi*. Out of 14 GRBs detected by the LAT until January 2010, 3 show clear evidence for a distinctive high energy ( $> \text{MeV}$  and up to the  $\text{GeV}$  range) spectral component, and another 8 show marginal evidence for such a component (Granot 2010). Thus, it is natural to deduce that the low energy photons (below and at the sub  $\text{MeV}$  peak of the flux) have a different origin than the higher energy (LAT) photons.

Out of the 3 bursts that show clear evidence for a distinct high energy spectral component, GRB090902B may be the easiest to analyse, for two reasons. First, the low energy part of the spectrum (the spectral peak) is very narrow, and both the low energy and high energy spectral slopes are very steep. Thus, any attempts of fitting the spectrum using the standard synchrotron-SSC model are rejected. On the other hand, the spectrum is easily fitted with a (multi-color) black body spectrum, plus an additional power law (Ryde *et al.* 2010). Second, the high energy power law component is spectrally distinctive from the low energy one. Using the opacity argument, the detection of a  $33.4 \text{ GeV}$  photon associated with this burst (Abdo *et al.* 2009a) implies that the emission radius of this photon must be much greater than the photosphere (see below). These two facts make this burst ideal for demonstrating how separation of the spectrum into thermal and non-thermal components enables one to deduce the physical conditions of the outflow at the emission sites of both the thermal and non-thermal photons. Moreover, as we will show below, one can use measurements of the non-thermal part, to remove some of the uncertainties that exist in measurements of the thermal component alone.

This paper is organized as follows. In section §2, we provide a general discussion on the properties of the thermal - non thermal model. We show how one can combine the hydrodynamic information derived by studying the properties of the thermal component with the constraints given by measuring the properties of the non-thermal part of the spectrum, to provide a comprehensive picture of the physical parameters at both emission sites. In §3 we demonstrate the use of our method by fitting the prompt emission spectrum of GRB090902B, and deducing its physical properties. We summarize and conclude in §4.

## 2. GENERAL PROPERTIES OF A THERMAL - NON-THERMAL MODEL

### 2.1. Temperature, luminosity and constraints on the value of $\epsilon_e$

We consider a fireball wind of total luminosity  $L$ , expanding from an initial radius  $r_0$  (which, for the sake of argument, can be assumed to be the last stable orbit around the central black hole, or the sonic radius; in any case, it is a few times the Schwarzschild radius around a non-rotating black hole). The initial black-body temperature at  $r_0$  is  $T_0 = (L/4\pi r_0^2 c a)^{1/4}$ , where  $c$  is the speed of light and  $a$  is the radiation constant. As the optically thick (adiabatic) wind expands, the baryon bulk Lorentz factor increases as  $\Gamma \propto r$ , and the comoving temperature drops as  $T' \propto r^{-1}$  (see, e.g., Mészáros

2006, for a comprehensive review).<sup>7</sup> As long as the wind remains optically thick, the acceleration continues until the plasma reaches the saturation radius,  $r_s = \eta r_0$ , above which  $\Gamma$  coasts to a value equal to the dimensionless entropy,  $\eta \equiv L/\dot{M}c^2$ . Here,  $\dot{M}$  is the mass outflow rate.

The photospheric radius is the radius above which the flow becomes optically thin to scattering by the baryon-related electrons. Depending on the values of the free model parameters ( $\eta$ ,  $L$ , and  $r_0$ ), this radius can be above or below the saturation radius (see Mészáros *et al.* 2002). For the parameter values characterizing GRBs (see below), the photospheric radius is above the saturation radius, and is given by (Abramowicz *et al.* 1991; Pe'er 2008)

$$r_{ph} = \frac{L\sigma_T}{8\pi m_p \eta^3 c^3} = 5.8 \times 10^{11} L \eta_3^{-3} \text{ cm}. \quad (1)$$

Here and below,  $\sigma_T$  is the Thomson cross section,  $m_p$  is the proton mass, and we use the convention  $Q = 10^x Q_x$  in cgs units. The high values of the luminosity and the Lorentz factor chosen for the demonstration in equation 1, are for ease of comparison with the *Fermi* results of GRB090902B (see §3 below).

Above the saturation radius, adiabatic energy losses (in the absence of dissipation) cause the temperature to drop as  $T = T_0 (r_s/r)^{-2/3}$ . The observed temperature of photons emitted at the photosphere is therefore

$$T^{ob} = T_0 \left( \frac{r_{ph}}{r_s} \right)^{-2/3} = 3.6 \times 10^5 (1+z)^{-1} L^{-5/12} \eta_3^{8/3} r_{0,8}^{1/6} \text{ eV}, \quad (2)$$

where  $z$  is the redshift. Note the very strong dependence of the observed temperature on the asymptotic value of the Lorentz factor,  $\eta$ : for high  $\eta$ , high values of the temperature are expected.

The observed photospheric thermal luminosity drops above the saturation radius as  $L_{Th}(r) = L(r/r_s)^{-2/3}$ , the greater part of the energy being in a kinetic form,  $L_k \sim L$  (Mészáros & Rees 2000; Rees & Mészáros 2005)<sup>8</sup>. The non-thermal part of the spectrum results from dissipation of the kinetic energy. Part of the dissipated energy goes into accelerating electrons, that radiate the non-thermal spectrum. Denoting by  $\epsilon_d$  the fraction of kinetic energy that is dissipated and by  $\epsilon_e$  the fraction of dissipated energy that is converted to energetic electrons, one obtains an *upper limit* on the ratio of non-thermal to thermal luminosity in the spectrum:

$$\frac{L_{NT}^{ob}}{L_{Th}^{ob}} \leq \epsilon_d \epsilon_e \left( \frac{r_{ph}}{r_s} \right)^{2/3} = 0.33 L^{2/3} \eta_3^{-8/3} r_{0,8}^{-2/3} \epsilon_{d,0} \epsilon_{e,-1}, \quad (3)$$

where the non-equality results from the fact that the electrons do not necessarily radiate 100% of their energy. Equation 3 implies an interesting result: *the higher the Lorentz factor of the flow is, the more pronounced its*

<sup>7</sup> From here on, quantities measured in the comoving frame are primed, while unprimed quantities are in the observer frame.

<sup>8</sup> Note that in fact at  $r > r_{ph}$  the kinetic luminosity is slightly higher due to energy conversion from the photons above the saturation radius. However, this is found to have a small effect on the parameter values, and is omitted for clarity.

thermal luminosity is expected to be. This result may be very significant given recent *Fermi*-LAT data, which show evidence for high values of the Lorentz factors in several bursts.

## 2.2. Initial expansion radius, photospheric radius and Lorentz factor

As was shown by Pe'er *et al.* (2007), the outflow parameters, in particular the Lorentz factor  $\eta$ , the initial expansion radius,  $r_0$  and the photospheric radius,  $r_{ph}$  can be inferred directly from studying the thermal component alone (for bursts with known redshift). For completeness of the analysis, we briefly repeat here the main arguments given by Pe'er *et al.* (2007).

The observed temperature of thermal photons emitted from the photosphere is  $T^{ob} \simeq 1.48\eta T'(r_{ph})/(1+z)$ <sup>9</sup>. Due to Lorentz aberration, the ratio  $(F_{Th}^{ob}/\sigma T^{ob4})^{1/2}$  is proportional to the photospheric radius divided by the Lorentz factor,

$$\mathcal{R} \equiv \left( \frac{F_{Th}^{ob}}{\sigma T^{ob4}} \right)^{1/2} = \xi \frac{(1+z)^2 r_{ph}}{d_L \eta}. \quad (4)$$

Here,  $\sigma$  is Stefan's constant,  $\xi$  is a geometrical factor of order unity,  $d_L$  is the luminosity distance and  $F_{Th}^{ob} = L_{Th}^{ob}/4\pi d_L^2$  is the observed thermal flux. Using the parametric dependence of  $r_{ph}$  from equation 1 in equation 4, one obtains the asymptotic Lorentz factor,

$$\eta = \left[ \xi(1+z)^2 d_L \frac{F_{Th}^{ob} \sigma_T}{2m_p c^3 \mathcal{R}} \right]^{1/4} \left( \frac{L}{L_{Th}^{ob}} \right)^{1/4}. \quad (5)$$

Combining this result with the equation for the observed thermal flux,  $L_{Th}^{ob} = L(r_{ph}/r_s)^{-2/3}$ , one obtains the initial expansion radius,

$$r_0 = \left( \frac{d_L \mathcal{R}}{\xi(1+z)^2} \right) \left( \frac{L}{L_{Th}^{ob}} \right)^{-3/2}, \quad (6)$$

and the photospheric radius,

$$r_{ph} = \left[ \frac{d_L^5 F_{Th}^{ob} \sigma_T \mathcal{R}^3}{\xi^3 (1+z)^6 2m_p c^3} \right]^{1/4} \left( \frac{L}{L_{Th}^{ob}} \right)^{1/4}. \quad (7)$$

The values of  $\eta$ ,  $r_0$  and  $r_{ph}$  are thus fully determined by the observed quantities of the thermal emission, up to the uncertainty in the luminosity ratio  $L/L_{Th}^{ob} \geq 1$ . Furthermore, equations 5 and 7 imply that the values of  $\eta$  and  $r_{ph}$  are not very sensitive to the uncertainty in this ratio.

Constraining the ratio  $L/L_{Th}^{ob}$  can most easily be done if an independent measurement of the kinetic energy exists. Such measurements are provided by studying the emission during the afterglow phase (Wijers & Galama 1999; Frail *et al.* 2001; Panaitescu & Kumar 2001; Freedman & Waxman 2001; Bloom *et al.* 2003; Berger *et al.* 2003; Nysewander *et al.* 2009), which provides good estimates of the kinetic energy remaining after the prompt emission phase. Fortunately, such measurements

<sup>9</sup> For photons emitted along the line of sight, the Doppler shift is  $\mathcal{D}(\theta=0) = 2\eta$ . The numerical factor 1.48 results from angular integration.

become ubiquitous, and are available for GRB090902B (Cenko *et al.* 2010); see further discussion in §3 below.

Even if afterglow measurements do not exist, the luminosity ratio  $L/L_{Th}^{ob}$  can still be constrained indirectly, in three independent methods. First, by fitting the non-thermal part of the spectrum, one obtains a constraint on  $\epsilon_d \epsilon_e (L/L_{Th}^{ob})$  (see eq. 3). Since  $\epsilon_d \epsilon_e < 1$ , a lower limit on  $L/L_{Th}^{ob}$  is obtained. Second, variability time measurements (if they exist) can constrain the initial expansion radius, since  $\delta t \geq r_0/c$ , which, in turn, provides an upper limit on the ratio  $L/L_{Th}^{ob}$  via equation 6. And finally, a high value of  $L_{Th}^{ob}$  implies that the luminosity ratio should not be high, in order to avoid an energy crisis.

## 2.3. Constraint on the emission radius of the non-thermal photons

Observations of high energy ( $\gtrsim 10$  GeV) photons by *Fermi*, are commonly used in the literature to constrain the Lorentz factors of GRB outflows, using the opacity argument. We point out though, that the constraints set in the literature are often based on an additional assumption, that is that the emission radius of the high energy photons,  $r_\gamma$  is connected to the Lorentz factor via  $r_\gamma = 2\eta^2 c \delta t$ , where  $\delta t$  is the variability time of the inner engine activity. This assumption, while true in the internal shocks model scenario, has two main drawbacks. First, it assumes an a-priori knowledge of the variability in the Lorentz factor, namely  $\Delta\eta \simeq \eta$  (this assumption translates into the numerical coefficient); and second, it relies on an assumed knowledge of the physical variability time,  $\delta t$ , which is difficult to be measured accurately.

A different approach was suggested by Zhang & Pe'er (2009): by releasing the requirement  $r_\gamma = 2\eta^2 c \delta t$ , it was shown that the opacity argument can be used to provide general constraints in the  $r_\gamma - \eta$  space. While this method does not provide directly the value of  $\eta$  (or of  $r_\gamma$ ), its main advantage is that it is not sensitive to the uncertainties mentioned above. Here, we take the arguments presented by Zhang & Pe'er (2009) one step forward. We first use the analysis of the thermal component to estimate the Lorentz factor  $\eta$ . At the second step, we use the constraints found by the opacity argument in the  $r_\gamma - \eta$  plane to deduce a lower limit on the emission radius of the non-thermal photons,  $r_\gamma$ .

The calculation is performed as follows. The cross section for pair production of photon with energy  $\epsilon_1$  is the highest for interactions with photons of energy  $\epsilon_2 = (m_e c^2)^2 / \epsilon_1$ . Therefore, considering the Lorentz boosting, a photon observed with energy  $\epsilon_{\max}^{ob} = 10 \epsilon_{\max,10}^{ob}$  GeV interacts mainly with photons having energies

$$\epsilon_1^{ob} \leq \frac{(m_e c^2)^2 \eta^2}{\epsilon_{\max}(1+z)^2} = \frac{26}{(1+z)^2} \eta_3^2 (\epsilon_{\max,10}^{ob})^{-1} \text{ MeV}. \quad (8)$$

This energy is about two orders of magnitude above the energy of the thermal photons (see eq. 2). We therefore do not expect the thermal photons to play a significant role in constraining the emission radius of the most energetic photons seen by the *Fermi*-LAT.

The observed spectrum above a few MeV is often modeled by a single power law,  $dN^{ob}/dt^{ob} dA d\epsilon^{ob} = f_0 \epsilon^{ob-\alpha}$ . For such a spectral fluence, the optical depth for pair production can be written as (Krolik & Pier 1991;

Woods & Loeb 1995; Lithwick & Sari 2001; Zhang & Pe'er 2009)

$$\tau_{\gamma\gamma} = \frac{\langle \sigma \rangle d_L^2 f_0 \delta t^{ob}}{r_\gamma^2 (1+z)^2} \frac{1}{\alpha - 1} \left[ \frac{(m_e c^2)^2}{\varepsilon_{\max}^{ob}} \right]^{1-\alpha} \left( \frac{\eta}{1+z} \right)^{2-2\alpha}. \quad (9)$$

Here,  $\langle \sigma \rangle$  is the cross section averaged over all angles; for flat energy spectrum ( $\alpha = 2$ ), one obtains  $\langle \sigma \rangle \approx \sigma_T/8$  (Svensson 1987; Gupta & Zhang 2008)<sup>10</sup>. Further note that  $\delta t^{ob}$  in equation 9 represents the observed time bin during which high energy photons are seen, and thus does not necessarily correspond directly to the uncertain physical variability time.<sup>11</sup>

For a flat energy spectrum ( $\alpha = 2$ ) observed between  $\varepsilon_{\min}$  and  $\varepsilon_{\max}$ <sup>12</sup>, the observed fluence is related to the (non thermal) luminosity via  $f_0 = L_{NT}^{ob}/4\pi d_L^2 \log(\varepsilon_{\max}/\varepsilon_{\min})$ . The requirement that the optical depth to pair production of the highest energy photon seen is smaller than unity, is translated into a lower limit on the emission radius,

$$r_\gamma \geq \left[ \frac{\langle \sigma \rangle L_{NT}^{ob} \delta t^{ob} \varepsilon_{\max}^{ob}}{4\pi \log(\varepsilon_{\max}/\varepsilon_{\min})} \right]^{1/2} \frac{1}{\eta m_e c^2} = 3 \times 10^{15} \text{ L}^{1/2} \delta t_0^{ob 1/2} \varepsilon_{\max,10}^{ob 1/2} \eta_3^{-1} \text{ cm}, \quad (10)$$

where  $\log(\varepsilon_{\max}/\varepsilon_{\min}) \approx 20$  was taken. For parameters characterizing GRBs seen by the LAT, the emission radius of the non-thermal photons is about 3 - 4 orders of magnitude larger than the photospheric radius (eq. 1), indicating that the observed spectrum must be emitted from (at least) two separate regions.

#### 2.4. The observed non-thermal spectrum: additional constraints on the free model parameters

The dissipation at  $r_\gamma$ , regardless of its exact nature, produces a population of energetic electrons. The energetic electrons emit the non-thermal part of the spectrum, by radiating their energy. There are three main radiative mechanisms responsible for the non-thermal emission: synchrotron emission, synchrotron-self Compton (SSC) emission and Comptonization of the thermal photons.

In order to estimate the relative contributions of the different emission mechanisms to the observed spectrum, we proceed in the following way.

##### 2.4.1. Electron energy loss by Comptonization of the thermal photons

The thermal photons serve as seed photons for Compton scattering by the energetic electrons. Their existence therefore contributes to the high energy part of the non-thermal spectrum.

The power emitted by Comptonization of the thermal photons (in the Thomson regime), relative to the power emitted as synchrotron radiation, is given by the ratio

<sup>10</sup> Note that this value is about twice the value presented in Lithwick & Sari (2001).

<sup>11</sup> E.g.,  $\delta t^{ob}$  could correspond to the integrated time over several distinct events.

<sup>12</sup> This assumption is taken here as it provides a good first order approximation to the observed high energy spectrum. A more accurate calculation considering the exact power law index will be used in §3.

of the energy density of the thermal photon field to the energy density in the magnetic field. At the photosphere, the (comoving) energy density of the thermal photons is  $u_{Th}(r_{ph}) = aT'(r_{ph})^4 = (L/4\pi r_s^2 c \eta^2)(r_{ph}/r_s)^{-8/3}$ . Since above the saturation radius the energy density of the photon field drops as  $u_{Th} \propto r^{-2}$ , at the dissipation radius  $r_\gamma$  it is equal to  $u_{Th}(r_\gamma) = (L/4\pi r_\gamma^2 \eta^2 c)(r_{ph}/r_s)^{-2/3}$ . The energy density in the magnetic field assumes a fraction  $\epsilon_B$  of the comoving energy density,  $L/4\pi r_\gamma^2 \eta^2 c$ . One therefore concludes that the ratio of the energy densities in the thermal photon and magnetic field is given by

$$\tilde{Y} \equiv \frac{u_{Th}}{u_B} = \frac{1}{\epsilon_B} \left( \frac{r_{ph}}{r_s} \right)^{-2/3} = 3 \text{ L}^{-2/3} \eta_3^{8/3} r_{0,8}^{2/3} \epsilon_{B,-1}^{-1} \quad (11)$$

It is thus clear that for parameters characterizing GRBs, the role played by Comptonization of thermal photons is, at the least, comparable to the role played by the synchrotron emission as a source of energy loss of the energetic electrons.

##### 2.4.2. Synchrotron spectrum

The dissipation process is expected to produce a power law distribution of energetic electrons with power law index  $p \gtrsim 2.0$ , above a characteristic Lorentz factor  $\gamma_m \simeq \epsilon_e (m_p/m_e) = 186 \epsilon_{e,-1}$ . Comparison of the cooling time to the dynamical time implies that the entire electron population is in the fast cooling regime: the cooling time is equal to the dynamical time for electrons having Lorentz factor  $\gamma_c = (3\pi m_e c^3 \eta^3 r_\gamma) / [\sigma_T \epsilon_B L (1 + Y + \tilde{Y})] = 3.5 (1 + Y + \tilde{Y})^{-1} \text{ L}^{-1} \eta_3^3 r_{\gamma,15} \epsilon_{B,-1}^{-1}$ . Here,  $Y$  has its usual meaning as the ratio of SSC to synchrotron radiated power,  $Y \equiv P_{SSC}/P_{syn}$ .

The peak of the synchrotron emission,  $\varepsilon_m^{ob} = (3/2) \hbar \eta / (1+z) (qB \gamma_m^2 / m_e c) = 1.5 (1+z)^{-1} \text{ L}^{1/2} \epsilon_{B,-1}^{1/2} r_{\gamma,15}^{-1} \epsilon_{e,-1}^2 \text{ keV}$ , is below the threshold energy of the *Fermi*-GBM detector. Here,  $q$  is the electron charge and  $B$  is the magnetic field at the dissipation radius. At the other end of the energy spectrum, comparison of the cooling time to the acceleration time provides an estimate of the maximum Lorentz factor of the accelerated electrons (assuming high efficiency in the acceleration process),  $\gamma_{\max} = [6\pi q / \sigma_T B (1 + Y + \tilde{Y})]^{1/2}$ . Synchrotron photons emitted by these electrons are expected at energies  $\varepsilon_{\max,syn}^{ob} = 240 (1+z)^{-1} \eta_3 (1 + Y + \tilde{Y})^{-1} \text{ GeV}$ , above the threshold energy for pair production, and above the maximum photon energy seen so far by *Fermi*. These results imply that synchrotron emission is expected to contribute to the spectrum at the entire spectral range covered by *Fermi*.

The fast cooling of the electrons imply that: (I) virtually all of the dissipated energy given to the electrons is radiated; and (II) for power law index  $p \approx 2.0$ , a flat energy spectrum ( $\nu F_\nu \propto \nu^0$ ) is expected from synchrotron emission over the entire energy range covered by *Fermi*. Note though that a high energy cutoff resulting from pair production can limit the maximum observed photon energy to values lower than  $\varepsilon_{\max,syn}^{ob}$  (see §2.3 above).

##### 2.4.3. Comptonization

There are two sources of Comptonized spectrum: Comptonization of the thermal photons, and SSC. At low energies, below the thermal peak, Comptonization is not a significant source of photons. Hence, the spectrum below the thermal peak is dominated by synchrotron emission. However, above the thermal peak, the three emission mechanisms- synchrotron, SSC and Comptonization of the thermal photons contribute in parts to the spectrum. As shown in equation 11 and is further discussed below, the relative contributions of the different emission mechanisms are of the same order of magnitude (in other words, both  $Y$  and  $\tilde{Y}$  are of the order unity). As a result, it is difficult to determine a single dominant emission mechanism at high energies. A consequence of this, is that the observed spectral index at high energies (at the LAT band, above the thermal peak) cannot be directly related to a power law index of the energetic electrons.

*Comptonization of the thermal emission.* Since  $(\gamma_m T')/m_e c^2 = 0.13 L^{-5/12} \eta_3^{5/3} r_{0.8}^{1/6} \epsilon_{e,-1} < 1$ , Comptonization of the thermal emission is in the Thomson limit. The Comptonized thermal photon spectrum has characteristic breaks similar to the SSC spectrum. Since the electrons are in the fast cooling regime, the Comptonized spectrum is expected to rise above  $\gamma_c^2 T^{ob} \gtrsim T^{ob}$  up to a peak at  $\epsilon_{Th}^{IC,ob} = (4/3) \gamma_m^2 (2.8 T^{ob}) \approx 50 (1+z)^{-1} L^{-5/12} \eta_3^{8/3} r_{0.8}^{1/6} \epsilon_{e,-1}^2$  GeV, roughly as  $\nu F_\nu \propto \nu^{1/2}$  (Sari & Esin 2001). At the highest energies, photons annihilate by producing pairs, a phenomenon which can explain the lack of detection of the 50 GeV photons so far.

*SSC.* The ratio of SSC to synchrotron luminosity is given by the parameter  $Y$ . For  $\epsilon_e \gg \epsilon_B$ , the value of  $Y$  can be approximated as  $Y \approx (\epsilon_e/\epsilon_B)^{1/2}$  (Sari & Esin 2001). A significant high-energy non-thermal part, as is seen by the *Fermi*-LAT, implies (via eq. 3), high value of  $\epsilon_e$ , close to equipartition. However, value of  $\epsilon_B > 10^{-2}$  as is inferred in many GRBs (see below), guarantees a value of  $Y$  of a few at most.

The SSC spectrum rises as  $\nu F_\nu \propto \nu^{1/2}$  below the peak of the SSC emission, which is expected at  $\epsilon_m^{IC,ob} = 2 \gamma_m^2 \epsilon_m^{ob} \approx 100 (1+z)^{-1} L^{1/2} \epsilon_{B,-1}^{1/2} \epsilon_{e,-1}^4 r_{\gamma,15}^{-1}$  MeV. At higher energies, the spectral shape follows a similar power law as the synchrotron spectrum, i.e., a flat energy spectrum is expected for  $p \approx 2$ .

The rise parts of both the thermal Comptonization and the SSC emission are independent of the power law index of the accelerated electrons. For power law index  $p \gtrsim 2.0$  a flat, or slightly decaying synchrotron spectrum is expected at the entire *Fermi* energy range (see §2.4.2 above). The combined effects of the flat synchrotron emission with the rise of the Comptonized spectrum therefore results in a mild increase in the total observed spectrum at high energies, above the thermal peak (see §3 below). Demonstration of spectral decomposition into its basic physical ingredients is presented in §A

The rising of the SSC component below  $\sim 100$  MeV, combined with the fact that the synchrotron spectrum is expected to be flat (or slightly inverted) and that  $Y$  is not expected to be much larger than a few, imply that at low energies (below the thermal peak), Comptoniza-

tion is not expected to play a significant role. The main emission mechanism below the thermal peak is therefore synchrotron emission. Since the *Fermi*-GBM detection range is above  $\epsilon_m^{ob}$ , the spectrum below the thermal peak is expected to be sensitive to the power law index of the accelerated electrons,  $p$ . Thus, measurement of the flux at low energies can provide an indication for both the values of  $\epsilon_B$  and of  $p$ .

Finally, we point out that the analysis carried in this section holds only as long as  $r_\gamma \gg r_{ph}$ . For  $r_\gamma \gtrsim r_{ph}$ , the effect of Comptonization is much more complicated due to the fact that the electrons cooling time is  $\propto r_\gamma$ . Therefore, for small dissipation radius, the cooling time is much faster than the dynamical time for all electron energies, and  $\gamma_c \gtrsim 1$ . For such rapid cooling, additional physical phenomena, that are not considered here, become important. Direct Compton scattering of the energetic photons provide the main source of heating, resulting in a quasi steady state distribution of mildly-relativistic electrons (Pe'er et al. 2005). Close to the photosphere, multiple Compton scattering by electrons in this quasi steady state produces a flat energy spectrum for a large region of parameter space (Pe'er et al. 2006).

### 3. DEMONSTRATION OF THE ANALYSIS METHOD: GRB090902B AS A CONCRETE EXAMPLE

The bright, long GRB090902B, which is one of the brightest bursts observed by LAT to date (Abdo et al. 2009a), provides an excellent example for demonstrating our analysis method. This is because of two very pronounced properties of its prompt emission spectrum. First, time resolved spectral analysis reveals a significant power law component in the LAT data (emission was observed up to 30 GeV), which is clearly distinct from the usual ‘‘Band’’ function used by Abdo et al. (2009a) to fit the spectrum in the sub-MeV range. Moreover, the fact that the high energy photons were delayed with respect to the photons at the sub MeV peak indicates a different origin. Second, the ‘‘Band’’ function used in fitting the sub MeV peak is extremely steep on both sides (low energy spectral slope  $n(\epsilon) \propto \epsilon^\alpha$ , with  $\alpha \approx -0.5..0$ , and high energy spectral slope  $\beta \approx -3..-5$ ), resulting in an unusually narrow peak. The steep spectral slopes seen in the sub-MeV range make it impossible to fit this spectrum with a model that contains only synchrotron and SSC.

On the other hand, both properties of the prompt spectrum fit perfectly into the framework suggested here: first, the sub-MeV peak is naturally modeled with the thermal emission component. While a single black body provides a sufficient fit, and is used to deduce the values of  $\eta$ ,  $r_0$  and  $r_{ph}$ , better fits are obtained with multi-color black body, as expected from a theoretical point of view (see further discussion below). Second, the non-thermal part (the high energy power law which extends to lower energies), can be easily explained by a combination of synchrotron, SSC and Comptonization of the thermal photons. Moreover, by doing so, we deduce the physical properties in the emission sites of both the thermal and non-thermal components, hence we obtain a comprehensive physical picture of the properties of this burst.

In the original analysis, Abdo et al. (2009a) separated the observed prompt emission into several time bins. The most restrictive constraints on the emission radius of the

non-thermal photons arise in time interval (c), 9.6–13.0 s from the trigger, since in this time interval an 11.16 GeV photon was observed. We therefore focus our analysis on this time interval.

### 3.1. Analysis of the thermal component: Lorentz factor, photospheric radius and dissipation radius

In order to deduce the value of the Lorentz factor by using the method presented in §2.2, one needs to fit the sub-MeV peak with a single black body spectrum, and study its properties (temperature and thermal flux). While this can be done for the data in time interval (c), since the properties of the outflow vary on a shorter time scale (variability time of  $\lesssim 0.1$  s was observed), smearing of the black body spectrum is expected. The shorter the time interval used for the fits, the higher the quality of the black body fits obtained. On the other hand, shorter time intervals result in lower quality of the high energy data, which is sparse.

We thus use time interval as short as possible to fit the narrow peak with a single black body, in order to deduce the hydrodynamics of the flow, and in particular obtain the Lorentz factor. We then use the longer time interval (the full time interval (c)) to study the properties of the non-thermal part of the spectrum. For the long time interval, we fit the spectral peak with a multicolor black body, which, as was shown by Ryde *et al.* (2010), provides better fits to the peak.

For the shorter time interval we use the results presented by Ryde *et al.* (2010), who showed that the narrow time interval, 11.008 – 11.392 s from the trigger, during which the 11.16 GeV photon is seen, provides sufficient data to analyze the sub-MeV spectral peak. During this time interval, the sub-MeV peak can be fitted with a single black body, with observed temperature  $T^{ob} = 168$  keV, and observed thermal flux  $F_{Th}^{ob} = 1.96 \times 10^{-5}$  erg cm $^{-2}$  s $^{-1}$ . Equation 4 thus implies a ratio  $\mathcal{R} = 1.55 \times 10^{-19}$  cm. At redshift  $z = 1.822$  (Cucchiara *et al.* 2009), the (isotropic-equivalent) thermal luminosity is  $L_{Th}^{ob} = 4\pi d_L^2 F_{Th}^{ob} = 4.6 \times 10^{53}$  erg s $^{-1}$ . Using  $\xi = 1.06$  in equations 5, 6 and 7 (Pe'er *et al.* 2007), one obtains  $\eta = 764 (L/L_{Th}^{ob})^{1/4}$ ,  $r_{ph} = 6.0 \times 10^{11} (L/L_{Th}^{ob})^{1/4}$  cm and  $r_0 = 7.9 \times 10^8 (L/L_{Th}^{ob})^{-3/2}$  cm.

Estimating the ratio  $(L/L_{Th}^{ob})$  is done in the following way. Due to the rapid cooling of the electrons, nearly 100% of the energy that is converted to the energetic electrons in the dissipation process is radiated in the form of non-thermal photons, that is  $L_{NT}^{ob} \simeq \epsilon_e \epsilon_d L$ . By fitting the non-thermal part of the spectrum, one obtains  $L_{NT}^{ob} \simeq 0.9 L_{Th}^{ob}$ , or  $\epsilon_e \epsilon_d \sim 0.9 (L_{Th}^{ob}/L)$  (see Figure 3.3). These fits are best done using a numerical simulation, since part of the dissipated energy is released outside the observed energy range of *Fermi*. After the main dissipation, the remaining kinetic luminosity,  $L_{AG} = L(1-\epsilon_d)$  is the available luminosity for the afterglow emission phase. As was found by Cenko *et al.* (2010), the energy release during the afterglow phase is  $\sim$  five times less than the energy release during the prompt emission phase. However, since the luminosity in time interval (c) is about twice the average luminosity during the prompt phase, we estimate the luminosity (thermal + non-thermal) in time interval (c) to be about ten times higher than the

luminosity during the afterglow phase,

$$\frac{L_{AG}}{L_{Th}^{ob} + L_{NT}^{ob}} = \frac{L(1-\epsilon_d)}{L_{Th}^{ob} + L\epsilon_e\epsilon_d} \approx \frac{1}{10}. \quad (12)$$

Using  $\epsilon_e \epsilon_d \sim 0.9 (L_{Th}^{ob}/L)$ , one obtains the luminosity ratio,

$$\frac{L_{Th}^{ob}}{L} \simeq \frac{10\epsilon_e}{1.9\epsilon_e + 9}. \quad (13)$$

For equipartition value,  $\epsilon_e = 0.33$ , one obtains  $L_{Th}^{ob}/L = 0.35$ , which imply  $\eta = 1000$  (and  $\epsilon_d = 0.93$ ). However, we consider this value as an upper limit, due to two reasons: first, this result implies very high total GRB luminosity,  $L = 1.3 \times 10^{54}$  erg s $^{-1}$ ; and second, using equation 6, it implies an initial expansion radius  $r_0 \simeq 1.6 \times 10^8$  cm, which translates into very short variability time,  $\delta t = r_0/c = 5$  ms. Using the extreme value  $\epsilon_e = 1$ , one obtains  $L_{Th}^{ob}/L = 0.92$ , or  $\eta = 780$ ,  $L = 5.0 \times 10^{53}$  erg s $^{-1}$ ,  $\epsilon_d = 0.83$  and  $r_0 \simeq 6.9 \times 10^8$  cm, which translates into physical variability time  $\delta t \approx 22$  ms.

We thus conclude, that the asymptotic value of the Lorentz factor is in the range  $780 \leq \eta \leq 1000$ , and the value of  $\epsilon_e$  is at or above equipartition. We further deduce that the photospheric radius is  $r_{ph} \simeq 6.1 - 7.8 \times 10^{11}$  cm, and that the dissipation efficiency is  $\epsilon_d \approx 85\% - 95\%$ . Using these values of  $\eta$  in equation 10, leads to the conclusion that the emission radius of the non-thermal photons is constrained,  $r_\gamma \geq 3.8 - 5.0 \times 10^{15}$  cm.

### 3.2. Numerical calculations: further constraints on the free model parameters

#### 3.2.1. The numerical model

As discussed in §2.4 above, following the dissipation process, simple analytical descriptions are insufficient to describe the spectrum, due to the roughly similar contributions from the different physical phenomena (synchrotron, SSC and thermal Comptonization), as well as the cutoff resulting from pair production. Therefore, in order to derive the spectral dependence on the different values of the free parameters, as well as confirm the analytical calculations presented above, we calculate numerically the photon and particle energy distribution for the different scenarios. In our calculations, we use the time-dependent numerical code presented in Pe'er & Waxman (2005). This code solved self-consistently the kinetic equations that determine the temporal evolution of  $e^\pm$  and photons, describing cyclo-synchrotron emission, synchrotron self absorption, direct and inverse Compton scattering, pair production and annihilation and the evolution of high energy cascade.

This code has two great advantages, which make it ideal in the study of the prompt spectra. First, it has a unique integrator, that enables solving the rate equations that govern the time evolution of the particles and photons energy distribution over the entire energy range. The code is able to calculate simultaneously processes happening over more than 15 orders of magnitude in time and energy ranges, thereby covering the entire spectral range, from radio up to the TeV band. The second advantage of the code is a full treatment of the various physical process, including the full cross sections (e.g., Klein Nishina effect is inherently taken into account; or that

for mildly relativistic electrons, the full cyclo-synchrotron emission spectrum is calculated; etc.).

In modeling the spectrum in time interval (c), the sub MeV peak is described as a multicolor black body spectrum, with varying amplitudes (Ryde *et al.* 2010):  $F_{Th}^{ob}(\nu; T_{max}) = \int_{T_{min}}^{T_{max}} (dA/dT) B_\nu(T) dT$ , where  $B_\nu(T) = (2h/c^2) \nu^3 / (e^{h\nu/T} - 1)$  is Planck function. The amplitude  $A(T)$  is temperature dependent,  $A(T) = A(T_{max})(T_{max}/T)^{q-4}$ , and is normalized such that the total flux is equal to the observed flux at the spectral peak,  $F_{Th}^{ob} = 1.82 \times 10^{-5} \text{ erg cm}^{-2} \text{ s}^{-1}$ . The normalization constant  $q$  and  $T_{max}$  are determined by fitting the spectrum,  $T_{max} = 328 \text{ keV}$  and  $q = 1.49$ .  $T_{min}$  cannot be determined, and its exact value is unimportant for the fits, as long as  $T_{min} \ll T_{max}$ .

In producing the spectrum, we assume that at radius  $r_\gamma$ , a fraction  $\epsilon_d$  of the kinetic energy is being dissipated (by an unspecified dissipation process). The energetic electrons, which assume a power law distribution with power law index  $p$ , carry a fraction  $\epsilon_e$  of the dissipated energy, and the magnetic field carries a fraction  $\epsilon_B$  of this energy. The multicolor black body spectra serve as background spectra for all the various processes (mainly Compton scattering by the energetic electrons, but also other processes such as, e.g., pair production). The code tracks the evolution of the spectrum, during the dynamical time. Here, we present the results at the end of time interval (c), i.e., we assume that the processes take place during an observed time of 3.4 seconds.

### 3.3. Numerical results

The numerical fits to the spectrum of GRB09092B at time interval (c), 9.6-13.0 seconds after the trigger, are presented in Figures 3.3 – 3.3. In Figure 3.3, we demonstrate the linear dependence of the non-thermal flux on the value of  $\epsilon_e$ . For the fits shown in this figure, we chose parameter values that fulfill the requirements in the previous sections and are typical for GRBs. Thus, we chose large dissipation radius,  $r_\gamma = 10^{17} \text{ cm}$ , strong magnetic field,  $\epsilon_B = 0.1$ , and electron power law index  $p = 2.0$ . The Lorentz factor was chosen to be  $\Gamma = 910$ , which implies  $L/L_{Th}^{ob} = 2.0$ , or  $L = 9.2 \times 10^{53} \text{ erg s}^{-1}$ . These values imply, via equation 13,  $\epsilon_e = 0.5$  and  $\epsilon_d = 0.9$ . The fit to the *Fermi* (GBM + LAT) data at time interval (c) appears as the solid (blue) line in Figure 3.3. We further added a scenario in which  $\epsilon_e$  is three times smaller ( $\epsilon_e = 0.17$ , dashed green line), which demonstrates the linear dependence of the non-thermal flux on the value of  $\epsilon_e$ . We point out that although a power law index  $p = 2.0$  was chosen, the combined effects of flat ( $\nu F_\nu \propto \nu^0$ ) synchrotron spectrum and rising ( $\nu F_\nu \propto \nu^{1/2}$ ) Comptonization spectrum, lead to a slight increase in the high energy spectral slope, which is consistent with the slope seen with *Fermi*.

In Figure 3.3, we consider different dissipation radii:  $r_\gamma = 10^{17} \text{ cm}$  (solid, blue),  $10^{16} \text{ cm}$  (dashed, green),  $10^{15.5} \text{ cm}$  (dash-dotted, red) and  $10^{15} \text{ cm}$  (dotted, purple). As the numerical code considers the full cross section for pair production, the numerical results are more accurate than the analytical approximations presented in §2.3, and can be used to validate them. The results presented in Figure 3.3 indeed confirm the main conclusion obtained analytically, that is that the observation of the

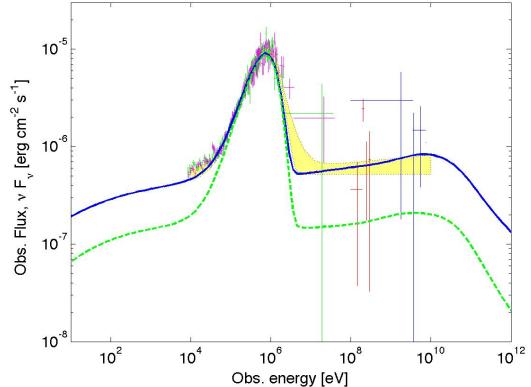


FIG. 1.— The dependence of the non-thermal flux on the fraction of energy given to the electrons,  $\epsilon_e$ . The data of GRB09092B are from the NaI (0,1), BGO(0,1) and LAT (back and front) detectors at time interval (c), 9.6 - 13.0 seconds after the GBM trigger. The light yellow shaded area show the  $\pm 1\sigma$  “Band” function fit to the data at this time interval (Abdo *et al.* 2009a). Parameter values chosen for the fits are: dissipation radius  $r_\gamma = 10^{17} \text{ cm}$ , bulk motion Lorentz factor  $\Gamma = 910$ , power law index of the accelerated electrons  $p = 2.0$ , GRB luminosity  $L = 9.2 \times 10^{53} \text{ erg s}^{-1}$  and fraction of dissipated kinetic energy  $\epsilon_d = 0.9$ . Shown are the simulation results for  $\epsilon_e = 0.5$  (blue, solid line), and  $\epsilon_e = 0.17$  (dashed, green line). The non-thermal flux is linear in the value of  $\epsilon_e$ .

11.16 GeV photon necessitates the dissipation radius to be above  $10^{15.5} \text{ cm}$ .

At larger radii, the high energy non-thermal part of the spectrum is not very sensitive to the exact dissipation radius. As shown in Figure 3.3, for dissipation radii  $r_\gamma \geq 10^{15.5} \text{ cm}$  it is possible to obtain numerical results which are within  $\pm 1\sigma$  errors of the empirical “Band” fit. In order to achieve this, high value of  $\epsilon_B$  and a slight tuning of the value of  $\epsilon_e$  is required. Thus, for  $r_\gamma = 10^{16} \text{ cm}$ , a value of  $\epsilon_e = 0.4$  was chosen, while for the other fits in this figure,  $\epsilon_e = 0.5$  was found adequate.

The numerical results show that the dependence of the pair production cutoff at high energies on  $r_\gamma$  is weaker than the analytical approximation presented in equation 10. The main reason for this is the contribution from the thermal photons, which is neglected in the derivation of equation 10. We can therefore conclude, that further constraints on the dissipation radius can not be obtained directly from the prompt spectrum, without additional assumptions. Finally, we point out that the small bump obtained in the scenario of  $r_\gamma = 10^{15} \text{ cm}$  at  $\Gamma m_e c^2 / (1+z) \simeq 150 \text{ MeV}$ , results from pair annihilation process, which is more pronounced at small dissipation radii due to the more rapid production of  $e^\pm$  pairs. Such a small bump is difficult to be observed, and indeed has not been observed so far. Moreover, since the Lorentz factor of the flow likely varies during the time interval considered here, it is expected to be smeared.

In Figures 3.3 and 3.3 we examine the dependence of the spectra on the uncertain values of the power law index of the energetic electrons and the fraction of dissipated energy carried by the magnetic field. In Figure 3.3, we consider three values of the power law index:  $p = 2.0$  (solid, blue),  $p = 2.2$  (dashed, green) and  $p = 2.5$  (dash-dotted, red). As explained in section 2.4.3 above, and is further demonstrated in appendix A, the high energy part of the spectrum (above the thermal peak) is gov-

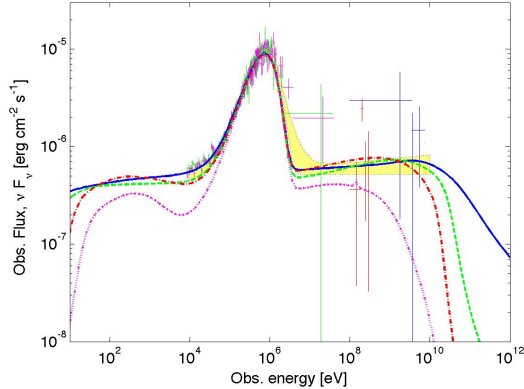


FIG. 2.— The dependence of the non-thermal flux on the dissipation radius,  $r_\gamma$ . We show the numerical results for dissipation occurring at  $r_\gamma = 10^{17}$  cm (solid, blue),  $10^{16}$  cm (dashed, green),  $10^{15.5}$  cm (dash-dotted, red) and  $10^{15}$  cm (dotted, purple), superimposed on the *Fermi* data and the  $\pm 1\sigma$  “Band” function fit to the data (light yellow shaded area). Values of  $\epsilon_B = 0.33$  and  $\epsilon_e = 0.5$  were chosen, apart from the fit for  $r_\gamma = 10^{16}$  cm, where  $\epsilon_e = 0.4$  is chosen. All the other parameters are the same as in Figure 1. Below  $10^{15.5}$  cm, pair production limits the maximum observed energy of photons to  $\lesssim$  GeV, and is thus inconsistent with the LAT observation of 11.16 GeV photon at this time interval.

erned by Compton scattering which is in the rising part of the spectrum (below  $\epsilon_m^{IC}$ ), and therefore the spectrum is not sensitive to the exact power law index of the accelerated electrons. We thus conclude that *observations at high energies cannot be used to constrain the power law index of the accelerated electrons*. On the other hand, the low energy part of the spectrum (below the thermal peak) is dominated by synchrotron emission, and is thus sensitive to the power law index of the electrons. Unfortunately, most of the effect is expected below the threshold energy of the *Fermi*-GBM detector, and therefore only weak observational constraints exist. We can therefore conclude that a power law index in the range  $2.0 \leq p \leq 2.2$  is consistent with the data, and even the higher value of  $p = 2.5$  can be consistent, however for such high power law index a somewhat fine tuning of the other model parameters (in particular, very high value of  $\epsilon_B$ , close to equipartition) is required.

Examination of the spectral dependence on the value of  $\epsilon_B$  is presented in Figure 3.3. The three fits presented in this figure, equipartition ( $\epsilon_B = 0.33$ ; solid, blue),  $\epsilon_B = 0.1$  (dashed, green) and  $\epsilon_B = 0.01$  (dash-dotted, red) show that the value of  $\epsilon_B$  cannot be too far below equipartition: low value of  $\epsilon_B$  results in a too low flux at low energies (below the thermal peak), which is inconsistent with the observation. It also leads to a more pronounced Compton peak, which is seen at the high energies. We can thus conclude that value of  $\epsilon_B$  close to equipartition is needed to be consistent with the observations. This high value justifies the need for numerical analysis, since although  $\epsilon_e$  is very high, both  $Y$  and  $\tilde{Y}$  are close to unity.

#### 4. SUMMARY AND DISCUSSION

In this paper, we considered the effect of thermal emission on the observed GRB prompt emission spectrum. Being a natural outcome of the GRB fireball model, thermal emission is an inherent part of the prompt emission

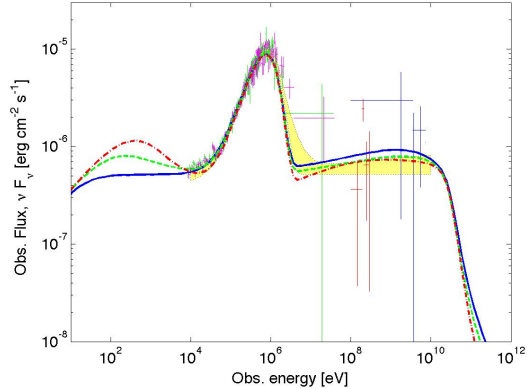


FIG. 3.— The dependence of the non-thermal flux on the power law index of the accelerated electron. On top of the *Fermi* data, shown are the numerical results for  $p = 2.0$  (solid, blue),  $p = 2.2$  (dashed, green) and  $p = 2.5$  (dash-dotted, red). Dissipation radius  $r_\gamma = 10^{16}$  cm,  $\epsilon_e = 0.5$ ,  $\epsilon_B = 0.33$  and all other parameter values same as in Figure 1 are chosen. The high energy spectrum is nearly insensitive to the exact value of  $p$  in the range considered,  $2.0 - 2.5$ . However, the low energy part (below the thermal peak) may provide indication for  $2.0 \leq p \leq 2.2$ .

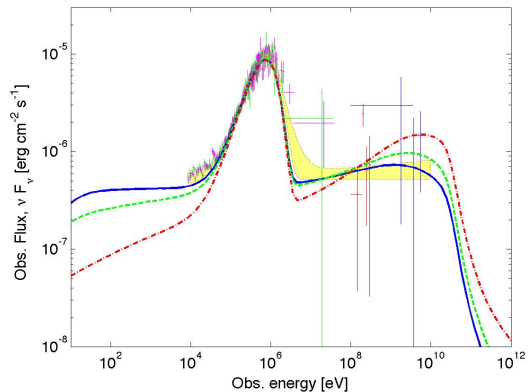


FIG. 4.— The dependence of the non-thermal flux on the fraction of energy carried by the magnetic field,  $\epsilon_B$ . Shown are the numerical results for equipartition ( $\epsilon_B = 0.33$ ; solid, blue),  $\epsilon_B = 0.1$  (dashed, green) and  $\epsilon_B = 0.01$  (dash-dotted, red). Dissipation radius  $r_\gamma = 10^{16}$  cm,  $\epsilon_e = 0.4$  and all other parameter values same as in figure 1 are chosen. While the effect of  $\epsilon_B$  on the high energy spectrum is minor, the low energy flux (below the thermal peak) necessitates high value of  $\epsilon_B$ , close to equipartition.

seen. As we showed in §2.1 (eq. 3), it is expected to be more pronounced for bursts with higher Lorentz factor. As we show here, *the inclusion of the thermal emission in the calculation of the prompt emission spectra, enables one to obtain a complete, self consistent physical model of the prompt emission spectrum seen over the entire FERMI energy range*. This is in contrast to the “Band” function fits, which do not carry any physical interpretation, and, in addition, require extra models to be able to fit the spectrum at high energies.

According to our model, the sub-MeV peak often seen is interpreted as being composed of multi-color black body emission from the photosphere. The non-thermal, high energy part seen in several bursts by the LAT instrument is interpreted as resulting from combined emission of synchrotron, SSC and Comptonization of the thermal

photons, following an episode of energy dissipation that occurs at large radius above the photosphere. Observations of high energy photons can be used to constrain the dissipation radius (eq. 10), which is clearly above the photospheric radius (eq. 1). Moreover, as we showed in §2.4, the relative contributions of synchrotron emission, SSC and Comptonization of the thermal photons, denoted by the parameters  $Y$  and  $\tilde{Y}$ , are expected to be of the same order of magnitude. Hence, the three emission mechanisms have roughly similar contributions to the high energy (above the thermal peak) part of the spectrum. This fact makes it difficult to directly determine the power law index of the accelerated electrons from measurements of the high energy spectral slope.

The separation made here between thermal and non-thermal emission, makes it possible to deduce the values of the free model parameters. First, by analyzing the photospheric part, one can deduce the value of the Lorentz factor, the initial expansion radius and the photospheric radius (see §2.2). Then, by analyzing the non-thermal part, one can constrain the dissipation radius,  $r_\gamma$  (eq. 10), and place constraints on the power law index of the accelerated electrons,  $p$ , and the strength of the magnetic field,  $\epsilon_B$ . By combining the fluxes of the thermal and non-thermal parts, one can further constrain the combined fractions of dissipated kinetic energy ( $\epsilon_d$ ) that is received by the energetic electrons ( $\epsilon_e$ ). Further separation of the values of these variables is more tricky, but can be done with the help of afterglow observations (see §3.1, eqs. 12, 13).

We demonstrated our analysis method on the bright, long GRB090902B. This burst is ideal for our demonstration purposes, because of the clear separation between the thermal and non thermal components seen, and the very pronounced thermal peak: both above and below the sub-MeV peak seen in this burst, the spectral slopes are too steep to enable fitting the spectrum with any combination of synchrotron and SSC emission models. However, as we showed in §3, Figures 3.3 – 3.3, excellent fits are obtained using the hybrid (thermal + non-thermal) model considered in this paper. By doing so, we were able to constrain the hydrodynamic properties of the outflow and the physical properties at the emission site: the initial expansion radius was found to be  $r_0 = 1.6 - 6.9 \times 10^8$  cm, the photospheric radius  $r_{ph} \simeq 6.1 - 7.8 \times 10^{11}$  cm and the Lorentz factor is in the range  $780 \leq \eta \leq 1000$ . The main source of uncertainty in these values is the unknown kinetic luminosity.

Fit results from the interval during which an 11.16 GeV photon was observed, constrain the dissipation radius to be  $r_\gamma \geq 3.8 - 5.0 \times 10^{15}$  cm. Combined measurements of the thermal and non-thermal parts imply very high dissipation efficiency,  $\epsilon_d \simeq 85\% - 95\%$ , and very high fraction of dissipated energy carried by the energetic electrons:  $\epsilon_e$  is at or above equipartition value. Measurements of the low energy part of the spectrum (below the thermal peak) imply high magnetic field,  $\epsilon_B$  close to equipartition. The power law index of the electrons is more difficult to constrain, as the high energy spectral slope *does not directly correspond to the power law index*. From the numerical fits, we concluded that  $2.0 \leq p \leq 2.2$  are consistent with the data, and that even  $p = 2.5$  is marginally consistent with the data.

The numerical results presented in Figure 3.3 show high energy cutoff due to pair production phenomenon. While this cutoff is consistent with the analytical prediction in equation 10, it also shows the limitation of the analytical approximations, which are commonly in use. Due to the inclusion of the thermal photons, the dependence of the cutoff energy on the emission radius is weaker than the simple approximation given in equation 10.

Additional constraints may be obtained by adding additional information, albeit with a higher level of uncertainty. For example, assuming the internal shocks scenario, and considering that the 11.16 GeV photon was seen after a delay of 11 s from the GBM trigger, implies, for constant Lorentz factor and  $\Delta\eta \simeq \eta$ , dissipation radius of  $r_\gamma \sim \eta^2 ct \approx 2 \times 10^{17}$  cm. We point out that this assumption is consistent with the observations, since the much more rapid variability time ( $\leq 0.1$  s) can be attributed to emission from the photosphere, rather than the high-energy non-thermal part.

While GRB090902B shows very pronounced peak and clearly separated high energy component, which make it ideal for demonstrating our analysis method, this is not the case in many GRBs. In fact, in many GRBs, the sub-MeV peak often seen is not as pronounced as in GRB090902B: the low and high energy spectral slopes are not as steep, and so in many cases pure single black body spectrum is too narrow to fit the sub MeV peak. However, there are two effects which are often being neglected. First, the fits are often made to *time integrated* spectra. As the properties of the outflow, in particular the Lorentz factor, vary on a very short duration (variation can be expected on time scale of the order of  $r_0/c$ , i.e.,  $\mathcal{O}(10\text{ms})$ ), the black body spectrum is often smeared. Even more than that, as was shown in Pe'er (2008), at any given instance, an observer sees simultaneously thermal photons emitted from different radii and different angles to the line of sight, hence having different Doppler shifts. As a result, the expected photospheric emission is *not* a pure black body, but a combination of black body spectra with different amplitudes. Thus, in fact, one expects to see a multi-color black body, as is indeed seen. The full theory of multi-color black body emission from relativistically expanding plasmas is currently in preparation [Pe'er & Ryde, in prep.].

The high energy spectral slope (above the thermal peak) often decays with a power law index much shallower than seen in GRB090902B. This, however, can be easily explained by Comptonization of the thermal photons, if the dissipation occurs close to the photosphere. As shown by Pe'er *et al.* (2005, 2006), in this scenario, multiple Compton scattering by electrons at a quasi steady state produces a flat energy spectra for a large parameter space region. Since the dissipation radius ( $r_\gamma$ ) can in principle take any value above the saturation radius, different dissipation radii can lead to very different observed spectra (see Pe'er *et al.* 2006). In fact, the uniqueness of GRB090902B lies in the fact that the dissipation radius  $r_\gamma \gg r_{ph}$ . Only because of this fact one is able to make the separation between the thermal and non-thermal parts of the spectrum, which are otherwise coupled.

The results of the fits to GRB090902B imply a very high value of  $\epsilon_e$ , close to or even above equipartition,

and an even higher value of  $\epsilon_d$ , 85%- 95%. These values are much higher than the values predicted by the internal shocks model: the typical efficiency in energy dissipation by internal shocks is no more than a few percent. The results obtain here (note that the exact nature of the dissipation process is not specified) thus raise another issue as to the validity of the internal shock model scenario. This is added to GRB080916C, in which detailed analysis by Zhang & Pe'er (2009) concluded that an additional source of energy must exist between the photospheric radius and the dissipation radius. The most plausible source of energy considered is magnetic, i.e., a Poynting dominated outflow (see Zhang & Yan 2010). We can con-

clude that the high efficiency required, may hint toward Poynting dominated outflow in the case of GRB090902B as well, and may even be a general requirement for all the bursts with pronounced high energy emission observed by LAT. A more generalized treatment of photospheric models with arbitrary magnetization is outside the scope of this manuscript, and is left for future work.

This research was supported by the Riccardo Giacconi Fellowship award of the Space Telescope Science Institute. AP wishes to thank Dale Frail, Jeremy Schnittman, Andy Fruchter, Kuntal Misra, Zeljka Bosnjak, Mario Livio and Kailash Sahu for useful discussions.

## APPENDIX

## DECOMPOSITION OF THE SPECTRUM INTO ITS BASIC PHYSICAL INGREDIENTS

The observed spectrum results from synchrotron emission, SSC and thermalization of the thermal photons, with a high energy cutoff resulting from pair production. As discussed in §3.2, the three emission processes are expected to have similar contributions to the observed spectrum of GRB090902B. Therefore, a “clean” decomposition into the spectral ingredients, as is presented in, e.g., Sari & Esin (2001), does not exist in practice.

The high energy spectral slope (above the thermal peak) does not have a direct correspondence to the power law index of the accelerated electrons. Therefore, a decomposition of the spectrum into the basic radiative processes can be useful in understanding the physical processes that shape the spectrum. Fortunately, such a decomposition can (up to some level) be done numerically.

The numerical results are presented in figure A, for dissipation radius  $r_\gamma = 10^{16}$  cm, and power law index  $p = 2.2$ . The dash-dotted (red) curve represents the spectrum that would have been obtained if only synchrotron emission was considered. As the cooling frequency is low, the spectral index in the entire *Fermi* range is  $\nu F_\nu \propto \nu^{1-p/2} \propto \nu^{-0.1}$ . When SSC is added (dashed, green curve) the spectral slope at low energies (below  $\approx 10^4$  eV) is not affected, while the spectrum at high energies becomes nearly flat. This results from a combination of a decreasing synchrotron flux and an increasing SSC flux. Note that in this scenario, the flux at low energies is weaker than the flux obtained for the pure synchrotron scenario, due to the fact that part of the electron energy is converted to SSC. Finally, the solid (blue) curve shows the combined effects when all the physical ingredients are added. Inclusion of the thermal photons does not affect the low energy spectral slope (below the thermal peak). However, Comptonization of the thermal photons contribute to the more pronounced spectrum at high energies. In addition, the inclusion of thermal photons leads to a sharper high energy cutoff, resulting from pair production.

## REFERENCES

- Abdo, A.A., *et al.* (The Fermi collaboration) 2009, *Science*, 323, 1688  
 Abdo, A.A., *et al.* (The Fermi collaboration) 2009, *ApJ*, 706, L138  
 Abdo, A.A., *et al.* (The Fermi collaboration) 2009, *Nature*, 462, 331  
 Abdo, A.A., *et al.* (The Fermi collaboration) 2010, *ApJ*, 712, 558  
 Abramowicz M.A., Novikov, I.D., & Paczyński, B. 1991, *ApJ*, 369, 175  
 Ackerman, M., *et al.* (The Fermi collaboration) 2010, *ApJ*, in press (arXiv:1005.2141)  
 Band, D., *et al.* 1993, *ApJ*, 413, 281  
 Berger, E., Kulkarni, S.R., & Frail, D. 2003, *ApJ*, 590, 379  
 Bloom, J.S., Frail, D. A., & Kulkarni, S.R. 2003, *ApJ*, 594, 674  
 Cenko, S.B., *et al.* 2010, *ApJ*, submitted (arXiv:1004.2900)  
 Crider, A., *et al.* 1997, *ApJ*, 479, L39  
 Crider, A., Liang, E.P., & Preece, R.D. 1998, *AIPC*, 28, 359  
 Cucchiara, A., Fox, D.B., Tanvir, N., & Berger, E. 2009, *GRB Coordinate Network*, 9873, 1  
 Daigne, F., Bosnjak, Z., & Dubus, G. 2009, in 2009 Fermi Symposium, eConf Proceedings C091122 (arXiv:0912.3743)  
 Daigne, F., & Mochkovitch, R. 2002, *MNRAS*, 336, 1271  
 Eichler, D., & Levinson, A. 2000, *ApJ*, 529, 146  
 Frail, D.A., *et al.* 2001, *ApJ*, 562, L55  
 Freedman, D.L., & Waxman, E. 2001, *ApJ*, 547, 922  
 Ghirlanda, G., Celotti, A., & Ghisellini, G. 2003, *A&A*, 406, 879  
 Ghisellini, G., & Celotti, A. 1999, *ApJ*, 511, L93  
 Giannios, D. *A&A* 457, 763  
 Giannios, D., & Spruit, H. 2005, *A&A*, 430, 1  
 Granot, J. 2010, in Proceedings of "The Shocking Universe - Gamma-Ray Bursts and High Energy Shock phenomena" (arXiv:1003.2452)  
 Guetta, D., & Granot, J. 2003, *ApJ*, 585, 885  
 Guetta, D., Spada, M., & Waxman, E. 2001, *ApJ*, 557, 399  
 Gupta, N., & Zhang, B. 2008, *MNRAS*, 384, L11  
 Kaneko, Y., *et al.* 2006, *ApJS*, 166, 298  
 Kaneko, Y., *et al.* 2008, *ApJ*, 677, 1168  
 Kobayashi, S., Piran, T., & Sari, R. 1997, *ApJ*, 490, 92  
 Krolik, J. H., & Pier, E.A. 1991, *ApJ*, 373, 277  
 Lazzati, D., Ghisellini, G., & Celotti, A. 1999, *ApJ*, 523, L113  
 Lazzati, D., Ghisellini, G., Celotti, A., & Rees, M.J. 2000, *ApJ*, 529, L17  
 Lazzati, D., Morsony, B.J., & Begelman, M.C. 2009, *ApJ*, 700, L47  
 Lithwick, Y., & Sari, R. 2001, *ApJ*, 555, 540  
 Medvedev, M.V. 2000, *ApJ*, 540, 704  
 Mészáros, P. 2006, *Rep. Prog. Phys.*, 69, 2259  
 Mészáros, P., Ramirez-Ruiz, E., Rees, M.J., & Zhang, B. 2002, *ApJ*, 578, 812  
 Mészáros, P., & Rees, M.J. 2000, *ApJ*, 530, 292  
 Mochkovitch, R., Maitia, V., & Marques, R. 1995, *Ap&SS*, 231, 441  
 Nysewander, M., Fruchter, A., & Pe'er, A. 2009, *ApJ*, 701, 824  
 Panaitescu, A., & Kumar, P. 2001, *ApJ*, 560, L49  
 Panaitescu, A., & Mészáros, P. 2000, *ApJ*, 544, L17  
 Pe'er, A., 2008, *ApJ*, 682, 463  
 Pe'er, A., Mészáros, P., & Rees, M.J. 2005, *ApJ*, 635, 476  
 Pe'er, A., Mészáros, P., & Rees, M.J. 2006, *ApJ*, 642, 995

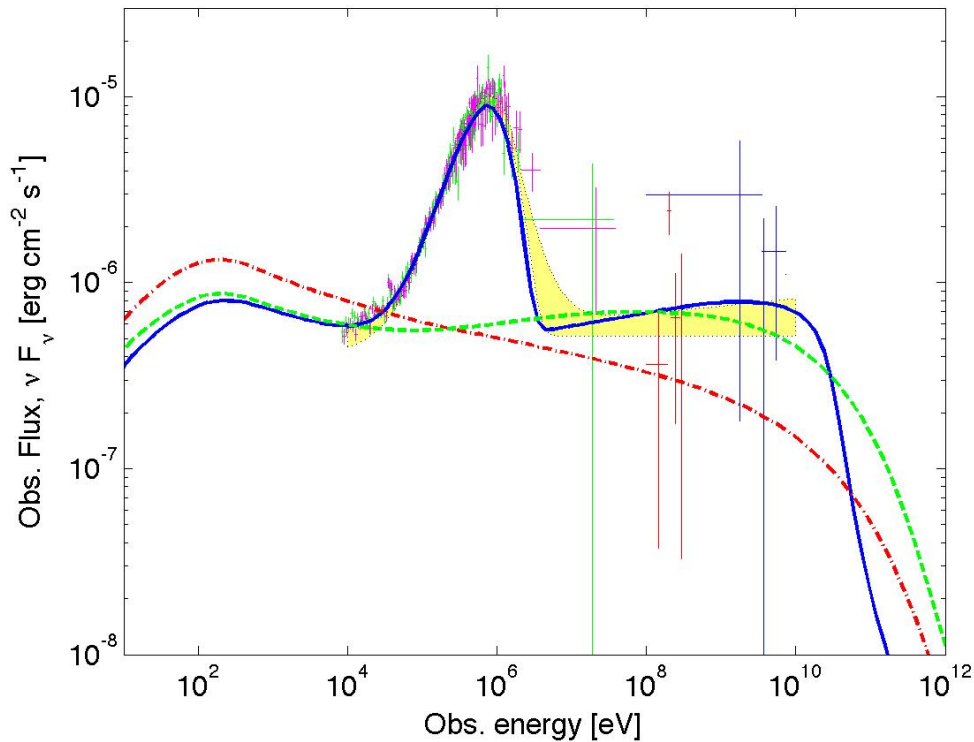


FIG. 5.— Demonstration of spectral decomposition into basic physical ingredients. The dash-dotted (red) curve show the spectrum that would have obtained if synchrotron radiation was the only source of emission. The dashed (green) curve show the resulting spectrum from synchrotron and SSC, and the solid (blue) curve show the spectrum with the full radiative ingredients (synchrotron, SSC and Comptonization of the thermal photons). Dissipation radius  $r_\gamma = 10^{16}$  cm,  $\epsilon_e = 0.5$ ,  $\epsilon_B = 0.33$ ,  $p = 2.2$  and all other parameter values same as in Figure 1 are chosen. The low energy spectral slope (below the thermal peak) is mainly due to synchrotron emission, and is thus sensitive to the power law index of the accelerated electrons. However, the high energy part (above the thermal peak) results from all of the radiative processes, and therefore cannot be used directly to constrain the values of the free model parameters.

Pe'er, A., Ryde, F., Wijers, R.A.M.J., Mészáros, P., & Rees, M.J. 2007, *ApJ*, 664, L1  
 Pe'er, A., & Waxman, E. 2004, *ApJ*, 613, 448  
 Pe'er, A., & Waxman, E. 2005, *ApJ*, 628, 857  
 Pe'er, A., & Zhang, B. 2006, *ApJ*, 653, 454  
 Pilla, R.P., & Loeb, A. 1998, *ApJ*, 494, L167  
 Piran, T. 2005, *Rev. Mod. Phys.* 76, 1143  
 Preece, R.D., *et al.* 1998, *ApJ*, 496, 849  
 Preece, R.D., *et al.* 1998, *ApJ*, 506, L23  
 Preece, R.D., *et al.* 2000, *ApJS*, 126, 19  
 Preece, R.D., *et al.* 2002, *ApJ*, 581, 1248  
 Rees, M.J., & Mészáros, P. 1994, *ApJ*, 430, L93  
 Rees, M.J., & Mészáros, P. 2005, *ApJ*, 628, 847  
 Ryde, F. 2004, *ApJ*, 614, 827  
 Ryde, F. 2005, *ApJ*, 625, L95  
 Ryde, F., & Pe'er, A. 2009, *ApJ*, 702, 1211  
 Ryde, F., *et al.* 2010, *ApJ*, 709, L172  
 Sari, R., & Esin, A.A. 2001, *ApJ*, 548, 787

Sari, R., & Piran, T. 1997, *MNRAS*, 287, 110  
 Sari, R., & Piran, T. 1997, *ApJ*, 485, 270  
 Shemi, A. 1994, *MNRAS*, 269, 1112  
 Spruit, H., Daigne, F., & Drenkhahn, G. 2001, *A&A*, 369, 694  
 Stern, B. E., & Poutanen, J. 2004, *MNRAS*, 352, L35  
 Svensson, R. 1987, *MNRAS*, 227, 403  
 Thompson, C. 1994, *MNRAS*, 270, 480  
 Toma, K., Wu, X.-F., & Mészáros, P. 2010, *ApJ*, submitted (arXiv:1002.2634)  
 Wijers, R.A.M.J., & Galama, T.J. 1999, *ApJ*, 523, 177  
 Woods, E., & Loeb, A. 1995, *ApJ*, 453, 583  
 Zdziarski, A.A., Svensson, R., & Paczyński, B. 1991, *ApJ*, 366, 343  
 Zhang, B., *et al.* 2007, *ApJ*, 655, 989  
 Zhang, B., & Pe'er, A. 2009, *ApJ*, 700, L65  
 Zhang, B., & Yan, H. 2010, *ApJ*, submitted